

Muon $g-2$ in a Type-X 2HDM assisted by inert scalars: probing at the LHC

Nabarun Chakrabarty*

*Department of Physics, Indian Institute of Technology Kanpur,
Kanpur-208016, Uttar Pradesh, India*

Abstract

A scenario augmenting the well known Type-X Two-Higgs doublet model (2HDM) with an additional inert doublet is proposed. The Type-X 2HDM is known to offer a solution to the muon $g-2$ anomaly for a light pseudoscalar. We show that the proposed framework can accomodate a heavier pseudoscalar on account of two-loop Barr-Zee (BZ) contributions to muon $g-2$ stemming from the inert doublet. We subsequently explore an interesting collider signal of this scenario in context of the 14 TeV LHC.

*Electronic address: nabarunc@iitk.res.in

I. INTRODUCTION

One of the experimental findings that continues to advocate dynamics beyond the Standard Model (SM) of particle physics is the longstanding muon $g-2$ anomaly. In a nutshell, a discrepancy has been noted between the SM prediction of the anomalous magnetic moment of the muon [1–11] and its experimental measurements made at BNL [12] and FNAL [13, 14]. The combined excess reported is

$$\Delta a_\mu \equiv a_\mu^{\text{exp}} - a_\mu^{\text{SM}} = 251(59) \times 10^{-11}. \quad (1)$$

A minimal extension of the SM long known to resolve the muon $g-2$ anomaly is the Type-X 2HDM. The model comprises an additional $SU(2)_L$ scalar doublet over and above SM. This entails an enlarged scalar sector, i.e., two CP-even neutral scalars h , H , a CP-odd neutral scalar A and a charged scalar H^\pm . A governing \mathbb{Z}_2 keeps flavour changing neutral current (FCNC) at bay by demanding that a particular fermion interacts with only one of the two doublets. This leads to several variants and one such is the Type-X 2HDM [15]. One important feature of the Type-X is that quark couplings to the additional scalars are suppressed while the ones with the leptons are enhanced. It is the enhanced leptonic couplings that potentially give rise to sizeable muon $g-2$ contributions at the one-loop and two-loop levels. A resolution of the anomaly thus becomes possible for a light pseudoscalar ($M_A \lesssim 100$ GeV) and high $\tan\beta$ ($\tan\beta \gtrsim 20$) [16–23]. As a perk, by virtue of the small quark couplings, such a parameter region in the Type-X evades stringent constraints from flavour observables and direct search from the colliders [24], especially the Large Hadron Collider (LHC). However, LHC searches for $h_{125} \rightarrow AA \rightarrow 4\tau, 2\tau 2\mu$ channels disfavor a large $\text{BR}(h_{125} \rightarrow AA)$ [25]. This strongly constrains the $M_A < 62.5$ GeV parameter region. Furthermore, the large $\tan\beta$ region also get restricted by lepton precision observables. A partial list of collider probes of the Type-X 2HDM is [26–30].

In this study, we seek to alleviate the aforementioned shortcomings by extending the scalar sector of the Type-X 2HDM so that additional two-loop Barr-Zee contributions are encountered¹. The smallest $SU(2)_L \times U(1)_Y$ multiplet for which there are additional Barr-Zee amplitudes is $(\mathbf{1}, Y)$. However, $Y \geq 2$ implies $Q \geq 0$, something not very attractive from the point of view of collider phenomenology when used in conjunction with a 2HDM that features scalars with $Q = 0, 1$ only. While $Y = 1$ is still an open possibility, production of one or more singly charged scalars at the colliders shall always lead to neutrinos in a leptonic cascade. This would eliminate the scope to directly look for the scalar via the invariant mass

¹ Some studies addressing the same problem using additional fermionic content and above the Type-X 2HDM are [31, 32]

handle. Neutral scalars could offer this enticing possibility and the lowest multiplet that features both charged and neutral scalars is $(\mathbf{2}, \frac{1}{2})$. We have therefore augmented the Type-X 2HDM with an additional scalar $SU(2)_L$ doublet. An extra \mathbb{Z}'_2 is imposed under which the new doublet is odd while all other fields are even. This addition can be deemed natural since the number of scalar doublets cannot be limited by the electroweak (EW) ρ -parameter or other fundamental constraints. While the \mathbb{Z}_2 is allowed to be broken by the scalar potential, \mathbb{Z}'_2 is *exact* and therefore disallows mixing between the third doublet with the first two. The third doublet thus remains *inert*. We refer to this scenario as (2+1)HDM and is therefore a generalisation of the popular inert doublet model (IDM).

The (2+1)HDM has generated some interest in the past. Reference [33] studied the constraints on this scenario from perturbative unitarity and oblique corrections. The reference [34] computed the strength of the $H^\pm W^\mp Z(\gamma)$ vertex at one-loop with a particular emphasis of the contribution coming from the inert doublet. A more recent study is [35] that computed various mono-object signals that arise as predictions of the model.

In this work, we have computed in detail the two-loop Barr-Zee contributions to Δa_μ stemming from the inert doublet. More precisely, we expect sizeable contributions from such loops owing to the possibility of large scalar trilinear couplings involving the inert scalars. We fold-in all relevant theoretical and experimental constraints in the process including dark matter direct detection. Our aim is to see if the (2+1)HDM can expand the parameter region in the $M_A - \tan\beta$ plane that is compliant with the muon g-2 excess.

The (2+1)HDM also predicts an interesting collider signal. The CP-even and CP-odd components can be pair produced at the LHC with following which the odd component can decay to the even component and A . Since, the A in this scenario can be potentially heavier than one in the Type-X 2HDM and still comply with Δa_μ , a lepton l coming from $A \rightarrow l^+ l^-$ ($l = \mu, \tau$ in this case) will accordingly have a higher transverse momentum in comparison to what is seen in case of the Type-X 2HDM. Moreover, The di-muon invariant mass now shall peak at a now higher M_A and the final state will also have a modified missing-transverse energy spectrum due to the presence of inert scalars. In all, the aforementioned kinematic features of this signal makes the (2+1)HDM discernible from the Type-X 2HDM. We have performed a detailed signal-background analysis in this work using both cut-based and multivariate techniques and estimated the observability at the 14 TeV LHC.

This study is segmented as follows. We introduce the (2+1)HDM scenario in Sect. II and elaborate all the constraints in Sect. III. The details of muon g-2 calculation can be found in Section IV. The collider analysis is given in Sect. V and we conclude in Sect. VI. Various important formulae are relegated to the Appendix.

II. THEORETICAL FRAMEWORK

The 2HDM framework that features two scalar doublets ϕ_1, ϕ_2 is augmented by an additional scalar doublet η . A discrete symmetry \mathbb{Z}_2 is introduced under which $\phi_{1,2} \rightarrow \phi_{1,2}$ while $\eta \rightarrow -\eta$. The most general scalar potential consistent with the gauge and discrete symmetries then reads:

$$V = V_2 + V_4^a + V_4^b, \quad (2a)$$

with

$$V_2 = -m_{11}^2|\phi_1|^2 - m_{22}^2|\phi_2|^2 + m_{12}^2(\phi_1^\dagger\phi_2 + \text{h.c.}) + \mu^2|\eta|^2, \quad (2b)$$

$$V_4^{\{\phi_1, \phi_2\}} = \frac{\lambda_1}{2}|\phi_1|^4 + \frac{\lambda_2}{2}|\phi_2|^4 + \lambda_3|\phi_1|^2|\phi_2|^2 + \lambda_4|\phi_1^\dagger\phi_2|^2 + \frac{\lambda_5}{2}[(\phi_1^\dagger\phi_2)^2 + \text{h.c.}] \\ + \lambda_6[(\phi_1^\dagger\phi_1)(\phi_1^\dagger\phi_2) + \text{h.c.}] + \lambda_7[(\phi_2^\dagger\phi_2)(\phi_1^\dagger\phi_2) + \text{h.c.}], \quad (2c)$$

$$V_4^{\{\phi_1, \phi_2, \eta\}} = \frac{\lambda'}{2}|\eta|^4 + \sum_{i=1,2} \left\{ \nu_i|\phi_i|^2|\eta|^2 + \omega_i|\phi_i^\dagger\eta|^2 + \left[\frac{\kappa_i}{2}(\phi_i^\dagger\eta)^2 + \text{h.c.} \right] \right\} \\ + [\sigma_1|\eta|^2\phi_1^\dagger\phi_2 + \sigma_2\phi_1^\dagger\eta\eta^\dagger\phi_2 + \sigma_3\phi_1^\dagger\eta\phi_2^\dagger\eta + \text{h.c.}]. \quad (2d)$$

In the above, V_2 combines all the dimension-2 operators of the scalar potential. The dimension-4 terms involving ϕ_1, ϕ_2 alone are given by $V_4^{\{\phi_1, \phi_2\}}$. Finally, the term $V_4^{\{\phi_1, \phi_2, \eta\}}$ comprises dimension-4 terms comprising all the three scalar doublets. All parameters in the scalar potential are chosen real to avoid CP-violation. The scalar doublets are parameterised below following electroweak symmetry breaking (EWSB):

$$\Phi_i = \begin{pmatrix} \phi_i^+ \\ \frac{1}{\sqrt{2}}(v_i + h_i + iz_i) \end{pmatrix}, (i = 1, 2), \quad \eta = \begin{pmatrix} \eta^+ \\ \frac{1}{\sqrt{2}}(\eta_R + i\eta_I) \end{pmatrix}, \quad (3)$$

where $v_{1,2}$ are the vacuum expectation values (VEVs) and $\tan\beta = \frac{v_2}{v_1}$. The non-inert particle spectrum in this case is identical with the 2HDM that consists of the neutral CP-even Higgses h, H , a CP-odd Higgs A and a charged Higgs H^\pm . The 2×2 mass matrix corresponding to the CP-even scalars is brought into a diagonal form by the action of a mixing angle α . Of these, the scalar h is taken to be the SM-like Higgs with mass 125 GeV.

The inert scalars coming from η do not mix with the ones from $\phi_{1,2}$ on account of the \mathbb{Z}_2 . The inert mass eigenstates are then η^+, η_R and η_I having the following squared masses:

$$m_{\eta^+}^2 = \mu^2 + \frac{1}{2}\{\nu_1 c_\beta^2 + \nu_2 s_\beta^2\}v^2 + \sigma_1 v^2 s_\beta c_\beta, \quad (4a)$$

$$m_{\eta_R}^2 = \mu^2 + \frac{1}{2}\{(\nu_1 + \omega_1 + \kappa_1)c_\beta^2 + (\nu_2 + \omega_2 + \kappa_2)s_\beta^2\}v^2 + (\sigma_1 + \sigma_2 + \sigma_3)v^2 s_\beta c_\beta, \quad (4b)$$

$$m_{\eta_I}^2 = \mu^2 + \frac{1}{2}\{(\nu_1 + \omega_1 - \kappa_1)c_\beta^2 + (\nu_2 + \omega_2 - \kappa_2)s_\beta^2\}v^2 + (\sigma_1 + \sigma_2 - \sigma_3)v^2 s_\beta c_\beta. \quad (4c)$$

	ξ_e^h	ξ_μ^h	ξ_τ^h	ξ_e^H	ξ_μ^H	ξ_τ^H	ξ_e^A	ξ_μ^A	ξ_τ^A
Lepton-specific	$-\frac{\sin\alpha}{\cos\beta}$	$-\frac{\sin\alpha}{\cos\beta}$	$-\frac{\sin\alpha}{\cos\beta}$	$\frac{\cos\alpha}{\cos\beta}$	$\frac{\cos\alpha}{\cos\beta}$	$\frac{\cos\alpha}{\cos\beta}$	$\tan\beta$	$\tan\beta$	$\tan\beta$
Muon-specific	$\frac{\cos\alpha}{\sin\beta}$	$-\frac{\sin\alpha}{\cos\beta}$	$\frac{\cos\alpha}{\sin\beta}$	$\frac{\sin\alpha}{\sin\beta}$	$\frac{\cos\alpha}{\cos\beta}$	$\frac{\sin\alpha}{\sin\beta}$	$-\cot\beta$	$\tan\beta$	$-\cot\beta$

TABLE I: Leptonic scale factors for the lepton- and muon-specific cases.

As for the Yukawa interactions, we adhere to the Type-X model in which case the Lagrangian reads

$$\mathcal{L}_Y = \mathcal{L}_Y^{\text{quark}} + \mathcal{L}_Y^{\text{lepton}} \quad (5a)$$

where

$$-\mathcal{L}_Y^{\text{quark}} = y_u \overline{Q}_L \tilde{\phi}_1 u_R + y_d \overline{Q}_L \phi_1 d_R + \text{h.c.}, \quad (5b)$$

$$-\mathcal{L}_Y^{\text{lepton}} = \sum_{l=e,\mu,\tau} \left[n_l^1 y_l \overline{Q}_L \phi_1 l_R + n_l^2 y_l \overline{Q}_L \phi_2 l_R + \text{h.c.} \right]. \quad (5c)$$

One has $n_{e,\mu,\tau}^1 = 0$ and $n_{e,\mu,\tau}^2 = 1$ for the lepton-specific case. On the other hand, there has also been some interest in a *muon-specific* type [36–38] where $n_{e,\tau}^1 = n_\mu^2 = 1$ while $n_\mu^1 = n_{e,\tau}^2 = 0$. Recasting in terms of the physical scalars, one has

$$\mathcal{L}_Y^{\text{lepton}} = \sum_{l=e,\mu,\tau} \frac{m_l}{v} \left(\xi_l^h h \bar{l} l + \xi_l^H H \bar{l} l - i \xi_l^A A \bar{l} \gamma_5 l + \left[\sqrt{2} \xi_l^A H^+ \bar{\nu}_l P_R l + \text{h.c.} \right] \right). \quad (6)$$

The ξ_l factors are tabulated below in Table I for the lepton-specific and muon-specific cases.

III. CONSTRAINTS

A. Theoretical constraints

The scalar potential remains perturbative if $|\lambda| < 4\pi$, $|y| < \sqrt{4\pi}$ where λ and y respectively denote a quartic and yukawa coupling of the theory.

The scalar potential remains positive definite along various directions in field space if the

following conditions are satisfied:

$$\lambda_1 > 0, \quad (7a)$$

$$\lambda_2 > 0, \quad (7b)$$

$$\lambda' > 0, \quad (7c)$$

$$\lambda_3 + \sqrt{\lambda_1 \lambda_2} > 0, \quad (7d)$$

$$\lambda_3 + \lambda_4 - |\lambda_5| + \sqrt{\lambda_1 \lambda_2} > 0, \quad (7e)$$

$$\nu_1 + \sqrt{\lambda_1 \lambda'} > 0, \quad (7f)$$

$$\nu_2 + \sqrt{\lambda_2 \lambda'} > 0, \quad (7g)$$

$$\nu_1 + \omega_1 - |\kappa_1| + \sqrt{\lambda_1 \lambda'} > 0, \quad (7h)$$

$$\nu_2 + \omega_2 - |\kappa_2| + \sqrt{\lambda_2 \lambda'} > 0. \quad (7i)$$

The perturbativity of the quartic couplings and the positivity of the scalar potential ultimately translate to as constraints on the more physical parameters, masses and mixing angles.

B. Oblique parameters

The NP corrections induced to the oblique parameters in this setup are can be split into a contribution coming from the active doublet ($\Delta X_{2\text{HDM}}$) and one from the inert doublet (ΔX_{IDM}).

$$\Delta X = \Delta X_{2\text{HDM}} + \Delta X_{\text{IDM}} \quad (8)$$

where $X = S, T, U$. The most constraining for scalar extensions of the SM is the T -parameter. The relevant expressions in the $\sin(\beta - \alpha) = 1$ limit are given below.

$$\Delta T_{2\text{HDM}} = \frac{1}{16\pi s_W^2 M_W^2} \left[F(m_{H^+}^2, m_H^2) + F(m_{H^+}^2, m_A^2) - F(m_H^2, m_A^2) \right], \quad (9a)$$

$$\Delta T_{\text{IDM}} = \frac{1}{16\pi s_W^2 M_W^2} \left[F(m_{\eta^+}^2, m_{\eta_R}^2) + F(m_{\eta^+}^2, m_{\eta_I}^2) - F(m_{\eta_R}^2, m_{\eta_I}^2) \right]. \quad (9b)$$

In the above,

$$\begin{aligned} F(x, y) &= \frac{x+y}{2} - \frac{xy}{x-y} \ln\left(\frac{x}{y}\right) \quad \text{for } x \neq y, \\ &= 0 \quad \text{for } x = y. \end{aligned} \quad (10)$$

The most updated bound reads [11]

$$\Delta T = 0.07 \pm 0.12. \quad (11)$$

We have imposed the stated bound have been at 2σ in our analysis.

C. Higgs signal strengths

We adhere to $\sin(\beta - \alpha) = 1$ in this work (known as the *alignment* limit in the context of 2HDMs) in which case the couplings of the fermions and gauge bosons to h become equal to the corresponding SM values. In this limit, the predicted values for the Higgs signal strength in the $b\bar{b}, \tau^+\tau^-, W^+W^-, ZZ, gg$ channels become consistent with the measurements at ATLAS and CMS. The only channel that can still deviate in this limit is $\gamma\gamma$ where the presence of the additional charged scalars H^+, η^+ leads to new one-loop contributions in the $h \rightarrow \gamma\gamma$ amplitude. One then has

$$M_{h \rightarrow \gamma\gamma}^{\text{NP}} = \sum_{\phi^+ = H^+, \eta^+} \frac{\lambda_{h\phi^+\phi^-} v}{2m_{\phi^+}^2} A_0\left(\frac{m_h^2}{4m_{\phi^+}^2}\right). \quad (12)$$

The total amplitude and the decay width then become

$$\mathcal{M}_{h \rightarrow \gamma\gamma} = \mathcal{M}_{h \rightarrow \gamma\gamma}^{\text{SM}} + \mathcal{M}_{h \rightarrow \gamma\gamma}^{\text{NP}}, \quad (13)$$

$$\Gamma_{h \rightarrow \gamma\gamma} = \frac{G_F \alpha^2 m_h^3}{128 \sqrt{2} \pi^3} |\mathcal{M}_{h \rightarrow \gamma\gamma}|^2. \quad (14)$$

where G_F is the Fermi constant. The various loop functions are listed below [39, 40].

$$A_{1/2}(x) = \frac{2}{x^2} ((x + (x-1)f(x))), \quad (15a)$$

$$A_1(x) = -\frac{1}{x^2} ((2x^2 + 3x + 3(2x-1)f(x))), \quad (15b)$$

$$A_0(x) = -\frac{1}{x^2} (x - f(x)), \quad (15c)$$

$$\begin{aligned} \text{with } f(x) &= \arcsin^2(\sqrt{x}); \quad x \leq 1 \\ &= -\frac{1}{4} \left[\log \frac{1 + \sqrt{1-x^{-1}}}{1 - \sqrt{1-x^{-1}}} - i\pi \right]^2; \quad x > 1. \end{aligned} \quad (15d)$$

The signal strength in the $\gamma\gamma$ channel is then given by

$$\mu_{\gamma\gamma} \simeq \frac{\Gamma_{h \rightarrow \gamma\gamma}}{\Gamma_{h \rightarrow \gamma\gamma}^{\text{exp}}}. \quad (16)$$

The latest 13 TeV results on the diphoton signal strength from the LHC read $\mu_{\gamma\gamma} = 0.99_{-0.14}^{+0.14}$ (ATLAS [41]) and $\mu_{\gamma\gamma} = 1.18_{-0.14}^{+0.17}$ (CMS [42]). Upon using the standard combination of signal strengths and uncertainties, we obtain $\mu_{\gamma\gamma} = 1.06 \pm 0.1$ and impose this constraint at 2σ .

D. Dark matter

The presence of the inert doublet protected by a discrete symmetry makes its neutral component (η_R or η_I) a DM candidate. The PLANCK collaboration quotes the following as

the latest measured value of the DM relic density [43]:

$$\Omega_{\text{Planck}} h^2 = 0.120 \pm 0.001 \quad (17)$$

The other important DM constraint comes from the search of DM-nucleon scattering cross sections by different terrestrial experiments such as XENON-1T [44, 45] and PANDA-X [46, 47]. The non-observation of such scatterings has led to upper limits on the DM-nucleon cross section with the most stringent bound for $m_{\text{DM}} < 1$ TeV coming from XENON-1T.

The model is implemented to the publicly available tool `micrOMEGAs` in order to compute the relic density and the spin-independent direct detection (SI-DD) cross section. The computed relic density is stipulated to be underabundant in this work as presence of other DM candidates (not accounted for in this work) is assumed. Folding-in a 10% experimental error in the measured central value, we demand

$$\Omega h^2 < 0.12 \pm 2 \times 0.012 \quad (18)$$

As for direct detection, we multiply the value obtained from `micrOMEGAs` by the ratio $\frac{\Omega}{\Omega_{\text{Planck}}}$. This ratio takes care of the fact that the present model accounts for only a part of the observed relic abundance. We define λ_{L_1} and λ_{L_2} below in lines similar to the IDM.

$$\lambda_{L_1} = \nu_1 + \omega_1 + k_1, \quad (19a)$$

$$\lambda_{L_2} = \nu_2 + \omega_2 + k_2. \quad (19b)$$

The $\eta_R - \eta_R - h$ coupling is given by $-\lambda_{L_1} v$ when only one active Higgs doublet is present. We mention in passing that the SI-DD scattering in this scenario proceeds via t-channel diagrams involving h and H .

IV. THE MUON $g - 2$ AMPLITUDE AND ITS NUMERICAL PREDICTION

We present an elaborate computation of Δa_μ in this section. The electromagnetic interaction of a lepton is given by

$$\bar{l}(p_2) \Gamma^\mu l(p_1) = \bar{l}(p_2) \left[\gamma^\mu F_1(q^2) + \frac{i \sigma^{\mu\nu} q_\nu F_2(q^2)}{2m_l} \right] l(p_1) \quad (20)$$

The lepton anomalous magnetic dipole moment is then defined as

$$a_l = F_2(0). \quad (21)$$

While giving the expressions for the various Δa_μ contributions in the (2+1)HDM, we denote the loop order in the superscript and the particle circulating in the loop in the subscript.

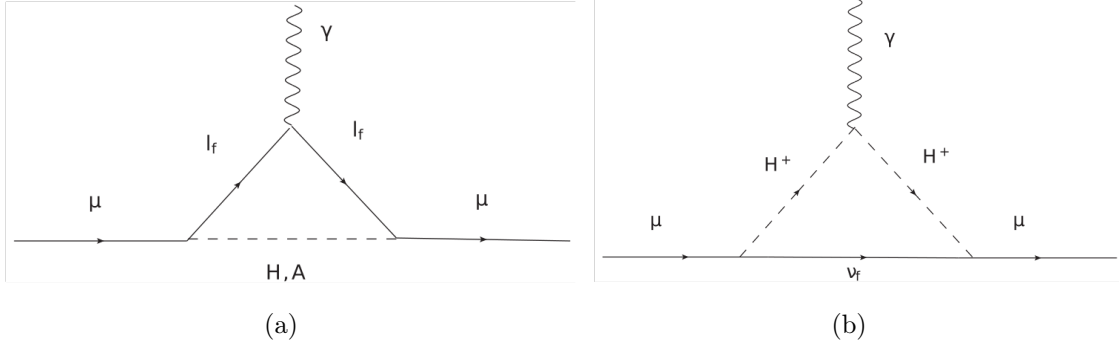


FIG. 1: One loop contributions to Δa_μ from (a) H, A and (b) H^+ .

The one-loop amplitudes in the alignment limit are given below:

$$\Delta a_{\mu(\phi)}^{(1l)} = \frac{M_\mu^2}{8\pi^2 v^2} \sum_{i=H,A} \frac{M_\mu^2}{M_{\phi_i^0}^2} (\xi_\mu^{\phi_i^0})^2 \int_0^1 dx \frac{x^2(2-x)}{\left(\frac{M_\mu^2}{M_{\phi_i^0}^2}\right) x^2 - x + 1}, \quad (22)$$

$$\Delta a_{\mu(H^+)}^{(1l)} = \frac{M_\mu^2}{8\pi^2 v^2} \left(\frac{M_\mu^2}{M_{H^+}^2}\right) (\xi_\mu^A)^2 \int_0^1 dx \frac{x^2(1-x)}{\left(\frac{M_\mu^2}{M_{H^+}^2}\right) x(1-x) - x}. \quad (23)$$

One notes that $\Delta a_{\mu(H^+)}^{(1l)} < 0$. The corresponding diagrams are shown in Fig.1.

The two-loop Barr-Zee contributions arise upon embedding $h\gamma\gamma, H\gamma\gamma, A\gamma\gamma$ and $H^+W^-\gamma$ form factors that themselves arise at one-loop, in a one-loop amplitude. The resulting topology is thus two-loop. We firstly list out the Feynman graphs that feature fermions in the one-loop form factors in Fig.2.

$$\begin{aligned} \Delta a_{\mu\{f, \phi\gamma\gamma\}}^{(2l)} &= \sum_f \frac{\alpha M_\mu^2}{4\pi^3 v^2} N_C^f Q_f^2 \xi_f^H \xi_\mu^H \mathcal{F}^{(1)} \left(\frac{M_f^2}{M_H^2} \right) \\ &\quad + \sum_f \frac{\alpha M_\mu^2}{4\pi^3 v^2} N_C^f Q_f^2 \xi_f^A \xi_\mu^A \tilde{\mathcal{F}}^{(1)} \left(\frac{M_f^2}{M_A^2} \right), \end{aligned} \quad (24a)$$

$$\begin{aligned} \Delta a_{\mu\{f, H^+W^-\gamma\}}^{(2l)} &= \frac{\alpha M_\mu^2 N_t |V_{tb}|^2}{32\pi^3 s_w^2 v^2 (M_{H^+}^2 - M_W^2)} \int_0^1 dx [Q_t x + Q_b(1-x)] \\ &\quad \times [\xi_d^A \xi_\mu^A M_b^2 x(1-x) + \xi_u^A \xi_\mu^A M_t^2 x(1+x)] \\ &\quad \times \left[\mathcal{G} \left(\frac{M_t^2}{M_{H^+}^2}, \frac{M_b^2}{M_{H^+}^2}, x \right) - \mathcal{G} \left(\frac{M_t^2}{M_W^2}, \frac{M_b^2}{M_W^2}, x \right) \right]. \end{aligned} \quad (24b)$$

Here, $N_C^f = 1(3)$ for leptons (quarks). Next to come are the two-loop amplitudes induced by the 2HDM scalars' running in the loops as shown in Fig.3. The corresponding amplitudes are expressed below.

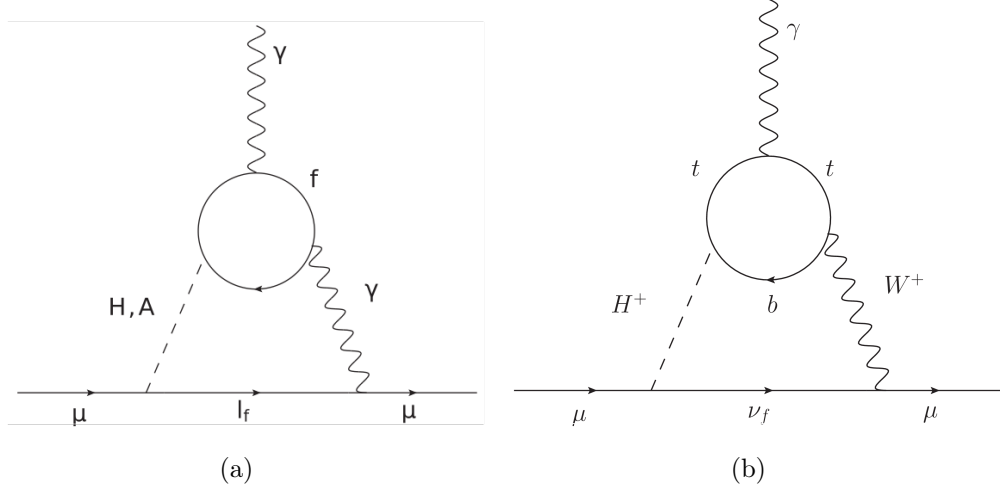


FIG. 2: Two loop contributions to Δa_μ from the fermions through (a) an effective $\phi\gamma\gamma$ vertex and (b) an effective $H^+W^-\gamma$ vertex.

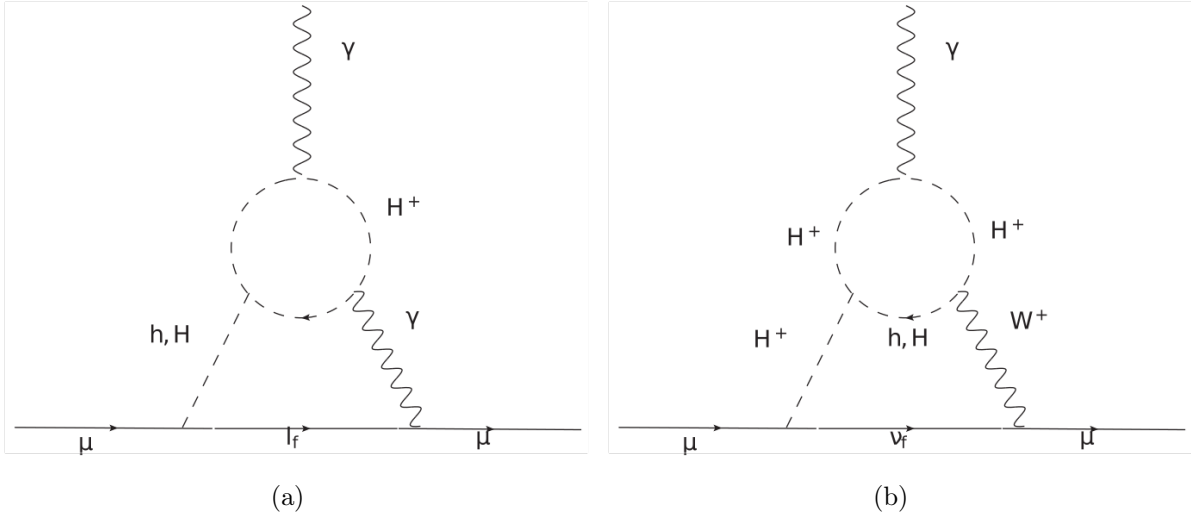


FIG. 3: Two loop contributions to Δa_μ from the 2HDM scalars through (a) an effective $\phi\gamma\gamma$ vertex and (b) an effective $H^+W^-\gamma$ vertex.

$$\Delta a_{\mu\{\phi, \phi\gamma\gamma\}}^{(2l)} = \sum_{j=h,H} \frac{\alpha M_\mu^2}{8\pi^3 M_{\phi_j^0}^2} \xi_\mu^{\phi_j^0} \lambda_{\phi_j^0 H^+ H^-} \mathcal{F}^{(2)} \left(\frac{M_{H^+}^2}{M_{\phi_j^0}^2} \right), \quad (25a)$$

$$\begin{aligned} \Delta a_{\mu\{\phi, H^+W^-\gamma\}}^{(2l)} &= \frac{\alpha M_\mu^2}{64\pi^3 s_w^2 (M_{H^+}^2 - M_W^2)} \sum_j \xi_\mu^{\phi_j^0} \lambda_{\phi_j^0 H^+ H^-} \int_0^1 dx x^2 (x-1) \\ &\times \left[\mathcal{G} \left(1, \frac{M_{\phi_j^0}^2}{M_{H^+}^2}, x \right) - \mathcal{G} \left(\frac{M_{H^+}^2}{M_W^2}, \frac{M_{\phi_j^0}^2}{M_W^2}, x \right) \right]. \end{aligned} \quad (25b)$$

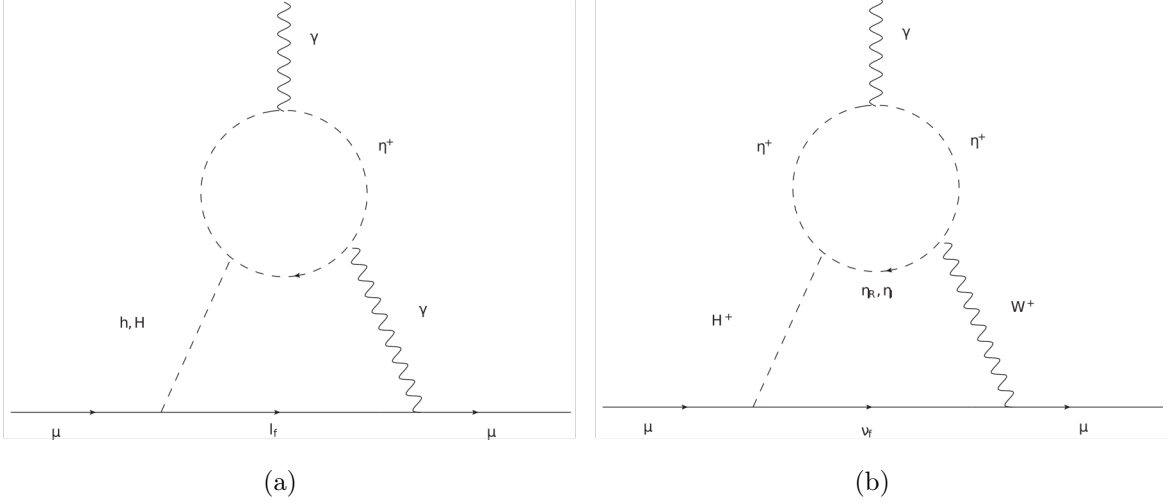


FIG. 4: Two loop contributions to Δa_μ from the inert scalars through (a) an effective $\phi\gamma\gamma$ vertex and (b) an effective $H^+W^-\gamma$ vertex.

Finally, Fig.4 depicts the contributions stemming from the inert scalars.

$$\Delta a_{\mu\{\eta, \phi\gamma\gamma\}}^{(2l)} = \sum_{j=h,H} \frac{\alpha M_\mu^2}{8\pi^3 M_{\phi_j^0}^2} \xi_\mu^{\phi_j^0} \lambda_{\phi_j^0 \eta^+ \eta^-} \mathcal{F}^{(2)} \left(\frac{M_{\eta^+}^2}{M_{\phi_j^0}^2} \right), \quad (26a)$$

$$\Delta a_{\mu\{\eta, H^+W^-\gamma\}}^{(2l)} = \frac{\alpha M_\mu^2}{64\pi^3 s_w^2 (M_{H^+}^2 - M_W^2)} \xi_\mu^A \lambda_{H^+ \eta^- \eta_R} \int_0^1 dx x^2 (x-1) \times \left[\mathcal{G} \left(\frac{M_{\eta^+}^2}{M_{H^+}^2}, \frac{M_{\eta_R}^2}{M_{H^+}^2}, x \right) - \mathcal{G} \left(\frac{M_{\eta^+}^2}{M_W^2}, \frac{M_{\eta_R}^2}{M_W^2}, x \right) \right] \quad (26b)$$

$$+ \frac{\alpha M_\mu^2}{64\pi^3 s_w^2 (M_{H^+}^2 - M_W^2)} \xi_\mu^A \lambda_{H^+ \eta^- \eta_I} \int_0^1 dx x^2 (x-1) \times \left[\mathcal{G} \left(\frac{M_{\eta^+}^2}{M_{H^+}^2}, \frac{M_{\eta_I}^2}{M_{H^+}^2}, x \right) - \mathcal{G} \left(\frac{M_{\eta^+}^2}{M_W^2}, \frac{M_{\eta_I}^2}{M_W^2}, x \right) \right]. \quad (26c)$$

Expressions for the relevant trilinear couplings and two-loop functions are given in Appendices A and B. Despite the additional loop suppression, the two-loop amplitude $\Delta a_{\mu\{f, \phi\gamma\gamma\}}$ in fact dominates over the one-loop contribution owing to the $\frac{M_f^2}{M_\mu^2}$ enhancement factor. The most important contributor in the lepton-specific case is the τ -loop that comes with a $\tan^2\beta \frac{M_\tau^2}{M_\mu^2}$ enhancement. An $\sim \mathcal{O}(10^{-9})$ contribution to Δa_μ can therefore be induced for high $\tan\beta$ and low M_A thereby paving way for a resolution of the anomaly. The largest two-loop fermionic contribution in case of the muon-specific case comes from the μ -loop. It must be added that $\Delta a_{\mu\{f, \phi\gamma\gamma\}}$ can also be sizeable in certain regions of the parameter space. More details about the purely 2HDM contribution can be found in [16–23].

The more important component of the present discussion is obviously the contribu-

tion coming from the sector added to the 2HDM, i.e., the inert scalars. Let us examine the trilinear coupling $\lambda_{H\eta^+\eta^-}$ more closely. For $\alpha = \beta - \frac{\pi}{2}$, the dominant behaviour is $\lambda_{H\eta^+\eta^-} \simeq \sigma_1 v (c_\beta^2 - s_\beta^2) \simeq \sigma_1 v$ for $\tan\beta \gtrsim 10$. Since σ_1 is not tightly constrained by the theoretical constraints on the scalar sector, $\lambda_{H\eta^+\eta^-}/v \sim \mathcal{O}(1)$ can lead to large values of $\Delta a_{\mu\{\eta, H\gamma\gamma\}}^{(2l)}$. A similar argument reveals that $\lambda_{H^+\eta^-\eta_R}/v$ and $\lambda_{H^+\eta^-\eta_I}/v$ can also take sizeable values while $\lambda_{h\eta^+\eta^-}$ remains suppressed for large $\tan\beta$. In all, large contributions to the muon g-2 prediction are expected to come from the inert doublet through $\Delta a_{\mu\{\eta, H\gamma\gamma\}}^{(2l)}$ and $\Delta a_{\mu\{\eta, H^+W^-\gamma\}}^{(2l)}$. A detailed numerical scan is required at this point to validate the model against the constraints. And this brings us to a counting of the independent model parameters. In the 2HDM sector, m_{11} and m_{22} are eliminated by the tadpole conditions: $\frac{\partial V}{\partial v_1} = \frac{\partial V}{\partial v_2} = 0$. The couplings λ_{1-5} can be expressed in terms of the physical masses, mixing angles and $\lambda_{6,7}$ using the following.

$$\lambda_1 = \frac{M_H^2 c_\alpha^2 + M_h^2 s_\alpha^2 - m_{12}^2 t_\beta}{v^2 c_\beta^2}, \quad (27a)$$

$$\lambda_2 = \frac{M_H^2 s_\alpha^2 + M_h^2 c_\alpha^2 - m_{12}^2/t_\beta}{v^2 s_\beta^2}, \quad (27b)$$

$$\lambda_3 = \frac{2M_{H^+}^2}{v^2} + \frac{s_{2\alpha}}{s_{2\beta}} \left(\frac{M_H^2 - M_h^2}{v^2} \right) - \frac{m_{12}^2}{v^2 s_\beta c_\beta}, \quad (27c)$$

$$\lambda_4 = \frac{M_A^2 - 2M_{H^+}^2}{v^2} + \frac{m_{12}^2}{v^2 s_\beta c_\beta}, \quad (27d)$$

$$\lambda_5 = \frac{m_{12}^2}{v^2 s_\beta c_\beta} - \frac{M_A^2}{v^2}. \quad (27e)$$

In the inert sector, $\mu, \omega_2, k_2, \nu_1, \nu_2$ can be traded off using

$$\mu^2 = M_{\eta_R}^2 - \frac{1}{2}\lambda_{L_1}v^2c_\beta^2 - \frac{1}{2}\lambda_{L_2}v^2s_\beta^2 - (\sigma_1 + \sigma_2 + \sigma_3)v^2s_\beta c_\beta, \quad (28a)$$

$$\omega_2 = \frac{M_{\eta_R}^2 + M_{\eta_I}^2 - 2M_{\eta^+}^2 + \omega_1v^2c_\beta^2 - 2\sigma_2v^2s_\beta c_\beta}{v^2s_\beta^2}, \quad (28b)$$

$$k_2 = \frac{M_{\eta_R}^2 - M_{\eta_I}^2 - k_1v^2c_\beta^2 - 2\sigma_3v^2s_\beta c_\beta}{v^2s_\beta^2}, \quad (28c)$$

$$\nu_1 = \lambda_{L_1} - \omega_1 - k_1, \quad (28d)$$

$$\nu_2 = \lambda_{L_2} - \omega_2 - k_2. \quad (28e)$$

With the alignment limit enforced through $\alpha = \beta - \frac{\pi}{2}$, the independent parameters in the (2+1)HDM are therefore $\{m_{12}, M_H, M_A, M_{H^+}, M_{\eta_R}, M_{\eta_I}, M_{\eta^+}, \tan\beta, \alpha, \lambda_6, \lambda_7, \omega_1, \kappa_1, \sigma_1, \sigma_2, \sigma_3, \lambda_{L_1}, \lambda_{L_2}\}$. We make

the following choice

$$\lambda_6 = \lambda_7 = \lambda_{L_1} = \lambda_{L_2} = 0.01, \quad (29a)$$

$$M_{H^+} = M_H = 150 \text{ GeV}, \quad (29b)$$

$$M_{\eta^+} = M_{\eta_R} + 1 \text{ GeV} = 100 \text{ GeV}, 200 \text{ GeV}. \quad (29c)$$

The low choice of the 2HDM masses in Eq. (29b) in Type-X 2HDM is consistent with various exclusion constraints [24] from the LHC on account of the suppressed couplings to quarks. On the other hand, the 1 GeV mass gap between η^+ and η_R as in Eq. (29c) disallows W -mediated inelastic direct detection scattering. Such choices of the mass splittings are aimed to minimise ΔT . The rest of the parameters are varied as follows.

$$0 < m_{12} < 500 \text{ GeV}, \quad (30a)$$

$$20 \text{ GeV} < M_A < 500 \text{ GeV}, \quad (30b)$$

$$10 < \tan\beta < 100, \quad (30c)$$

$$|\omega_1|, |\kappa_1| < 4\pi, \quad (30d)$$

$$|\sigma_1|, |\sigma_2|, |\sigma_3| < 2\pi, \quad (30e)$$

$$|M_{\eta_I} - M_{\eta_R}| < 500 \text{ GeV}. \quad (30f)$$

The parameter points passing all the constraints are plotted in the $M_A - \tan\beta$ plane in Fig.5. The most important finding to emerge is that the parameter space compatible with the observed muon g-2 excess appreciably expands in presence of an additional inert scalar doublet. An $M_A = 300 \text{ GeV}$ is now allowed for $\tan\beta \simeq 35$ (70) for $M_{\eta^+} = 100$ (200) GeV for the lepton-specific case. This enhancement is in fact more accentuated as shown in Fig.6 for the muon-specific case. And this is because $\Delta a_{\mu_{\{f, \phi\gamma\gamma}}^{(2l)}}$ is smaller compared to the lepton-specific case owing to the suppressed τ -Yukawa couplings. The only enhanced amplitude comes from the μ -loop. The muon specific 2HDM accordingly predicts $M_A \lesssim 50 \text{ GeV}$ for the entire $\tan\beta$ range taken. In all, a much heavier A get allowed in the (2+1)HDM for both lepton- and muon-specific Yukawa couplings.

V. COLLIDER SIGNALS

This section demonstrates the testability of the given framework at the 14 TeV LHC. And we use both cut-based and multivariate analyses towards doing that. While signatures of the pseudoscalar A decaying to $\tau^+\tau^-$ in context of the Type-X 2HDM have been looked at in the literature, we remind that the value of Δa_μ in the stipulated band demands an appropriately light A , that is, $M_A \lesssim 100 \text{ GeV}$. On the other hand, the present scenario allows

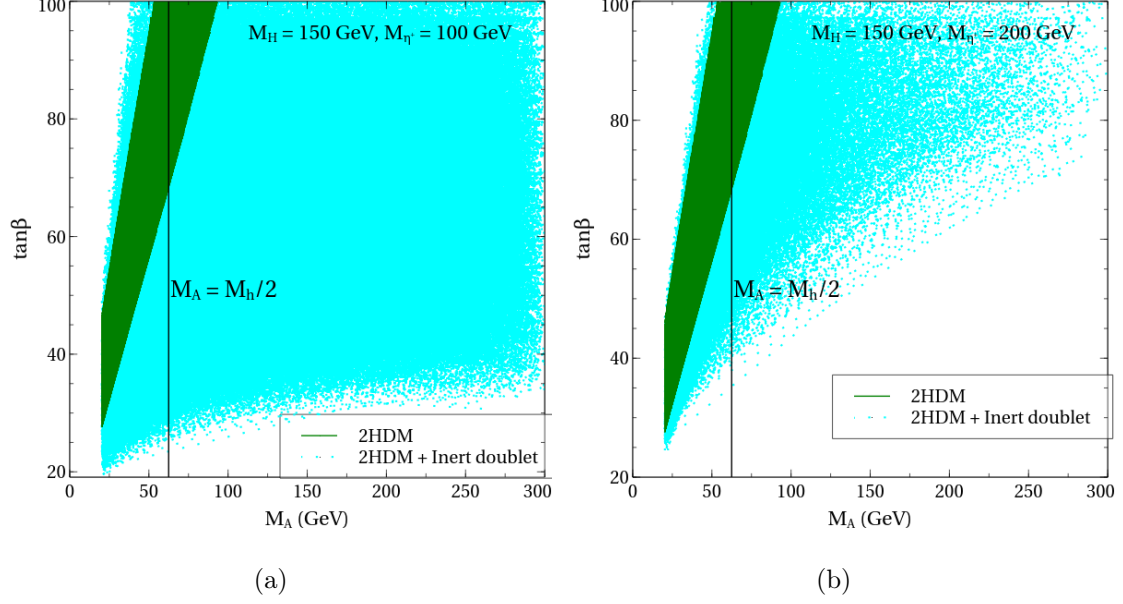


FIG. 5: The parameter space compatible with the observed Δa_μ in case of a lepton-specific 2HDM for $M_{\eta^+} =$ (a) 100 GeV and (b) 200 GeV. The color-coding is explained in the legends. The region to the left of the vertical line is tightly constrained by $\text{BR}(h \rightarrow AA)$ measurements.

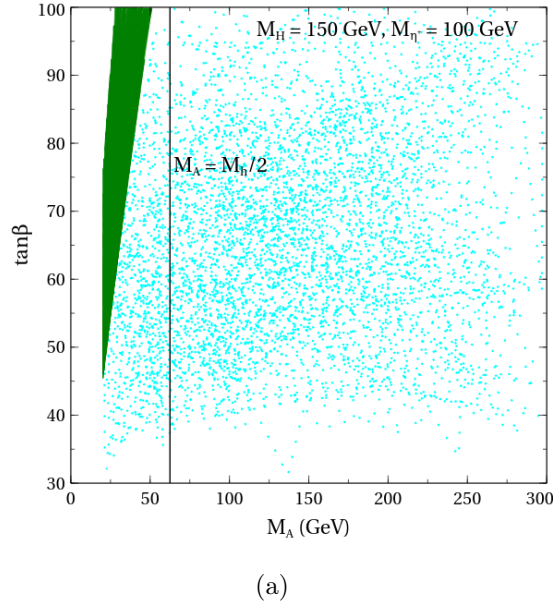


FIG. 6: The parameter space compatible with the observed Δa_μ in case of a muon-specific 2HDM for $M_{\eta^+} = 100$ GeV. The color-coding is explained in the legends. The region to the left of the vertical line is tightly constrained by $\text{BR}(h \rightarrow AA)$ measurements.

	BP1	BP2	BP3
m_{12}	17.80 GeV	17.20 GeV	19.60 GeV
$\tan\beta$	70.75	75.79	58.24
M_A	144.88 GeV	168.96	220.76
M_{η_I}	300.50 GeV	419.00 GeV	478.50 GeV
k_1	-3.84	-7.69062	-6.50
ω_1	-8.46	-3.09133	-1.75
σ_1	-4.15	-4.68726	-6.23
σ_2	0.33	5.15221	3.09
σ_3	6.20	3.74478	-5.76
Δa_μ	1.74	2.78203	1.54
σ_{SI}^{eff}	$6.36 \times 10^{-46} \text{ cm}^2$	$1.22 \times 10^{-47} \text{ cm}^2$	$6.60 \times 10^{-47} \text{ cm}^2$
$\text{BR}(\eta_I \rightarrow \eta_R A)$	0.91	0.71	0.76
$\text{BR}(A \rightarrow \mu^+ \mu^-)$	0.99	0.99	0.99

TABLE II: Benchmark points used for studying the discovery prospects of an A in the (2+1)HDM. The values for the rest of the masses are $M_H = M_{H^\pm} = 150 \text{ GeV}$, $M_{\eta^\pm} = M_{\eta_R} + 1 \text{ GeV} = 100 \text{ GeV}$.

for a much heavier A that is compliant with Δa_μ . This implies that the lepton pair coming from the decay of A would be more boosted than they would be in case of the Type-X. In addition, the decay $A \rightarrow \mu^+ \mu^-$, for instance, would enable an efficient identification of the events owing to a clean di-muon invariant mass ($M_{\text{inv}}^{\mu\mu}$) peaking around M_A . Such a decay can potentially be the 'smoking gun' signal for a light spin-0 resonance.

Motivated by the above, we therefore propose the following signal for the muon-specific case:

$$pp \rightarrow \eta_R \eta_I \rightarrow \eta_R \eta_I A \rightarrow \mu^+ \mu^- + \cancel{E}_T$$

That is, an $\eta_R \eta_I$ pair is dominantly produced via an s-channel exchange of Z . The small contribution from A -exchange can be neglected. Following a $\eta_I \rightarrow \eta_R A$ decay, the A subsequently decays to a $\mu^+ \mu^-$ pair. The lightest inert scalar η_R registers as missing transverse momentum (\cancel{E}_T). Thus, a modified \cancel{E}_T spectrum *w.r.t.* the SM is yet another handle to discern the signal from the background. We put forth the following benchmark points (in Table II) to probe the observability of A at the 14 TeV LHC. The BPs satisfy all the applied constraints and predict the requisite value of Δa_μ , as can be read from Table II. All the three BPs are characterised by (i) $M_{\eta_I} > M_{\eta_R} + M_A$, and (ii) $\text{BR}(A \rightarrow \mu^+ \mu^-) \sim 100\%$. While (i) ensures that the $\eta_I \rightarrow \eta_R A$ mode is kinematically open, (ii) can be straightforwardly understood as a consequence of other possible decay modes of A such as $A \rightarrow ZH, W^\pm H^\mp$

Signal/Backgrounds	Process	Cross section
Signal		
BP1		13.36 fb
BP2	$pp \rightarrow \eta_R \eta_I \rightarrow \eta_R \eta_R A \rightarrow \mu^+ \mu^- + \cancel{E}_T$	3.43 fb
BP3		2.28 fb
Backgrounds		
	$pp \rightarrow l^+ l^- + \cancel{E}_T$	2.08×10^3 fb
	$pp \rightarrow t\bar{t} \rightarrow b\bar{b} W^+ W^- \rightarrow l^+ l^- b\bar{b} + \cancel{E}_T$	3.09×10^4 fb
	$pp \rightarrow W^\pm Z \rightarrow l^+ l^- l^\pm + \cancel{E}_T$	1.71×10^2 fb

TABLE III: Signal and background cross sections at the 14 TeV LHC.

remaining kinematically closed.

The primary background is $pp \rightarrow l^+ l^- + \cancel{E}_T$ that mainly comes from $pp \rightarrow W^+ W^-$, ZZ . Owing to the large $pp \rightarrow t\bar{t}$ cross section, the $pp \rightarrow t\bar{t} \rightarrow l^+ l^- b\bar{b} + \cancel{E}_T$ process can also lead to a sizeable background when both the b -jets are missed. A small contribution also comes from $pp \rightarrow W^\pm Z \rightarrow l^+ l^- l^\pm + \cancel{E}_T$ when one lepton is missed. The cross sections of the signal BPs and the backgrounds are given in Table III. We have used MG5aMC@NLO [48] to generate the signal and background events at the leading order (LO). The CTEQ6L Parton Distribution Function (PDF) set and default hadronization and factorization scales are used. The parton level events are passed on to pythia8 [49] for showering and hadronization and subsequently to Delphes-3.4.1 for detector simulation. Specifically, we have throughout used the default CMS detector simulation card that comes with Delphes-3.4.1 [50]. For an integrated luminosity L , the number in a signal or background sample of events is determined as $L \times \sigma \times \epsilon$ with σ and ϵ respectively referring to the cross section and cut-efficiency. The signal significance is computed using the formula $S = \sqrt{\left[(N_S + N_B) \log\left(\frac{N_S + N_B}{N_B}\right) - N_S \right]}$ [51] where N_S (N_B) denotes the number of signal (background) events.

Events are selected by demanding exactly two opposite sign muons and zero b -jets. Sizeable background fractions are eliminated at this level itself since the background processes in this case mostly lead to flavor-democratic leptons. In addition to this demand, the following trigger-level cuts are also applied:

$$p_T^l > 10 \text{ GeV}, p_T^l > 10 \text{ GeV}, |\eta_{j,l}| < 2.5, \Delta R_{ll} > 0.2, \Delta R_{lj} > 0.2, \Delta R_{jj} > 0.4. \quad (31)$$

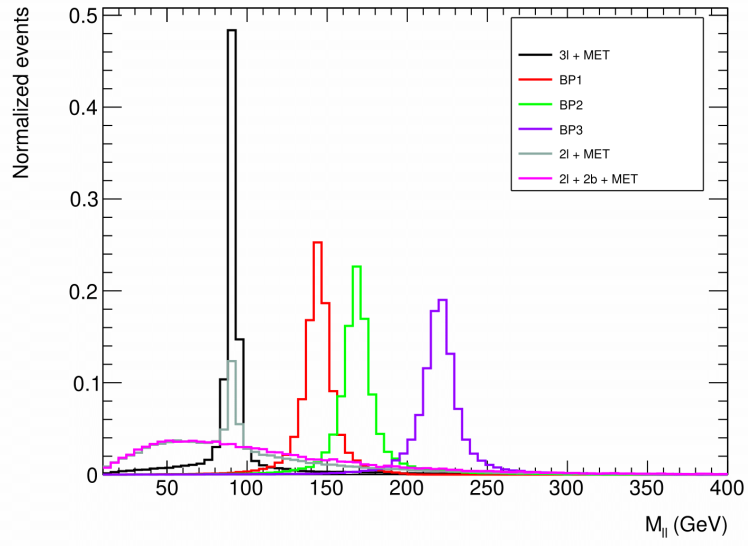
In the above, $l = e, \mu$ and j corresponds to a light jet. It is reminded that light jets come only from showering for the signal and backgrounds in this case. For the cut-based analysis, we first identify the following kinematic variables of interest: $M_{\text{inv}}^{\mu\mu}$, $p_T^{\mu_1}$ and \cancel{E}_T where μ_1 refers to the leading muon. The normalised distributions of the three variables are shown

in Fig.7. The corresponding selection cuts on these variables are denoted by C_1 , C_2 and C_3 respectively. The ensuing discussion explains the distributions and motivates the cuts.

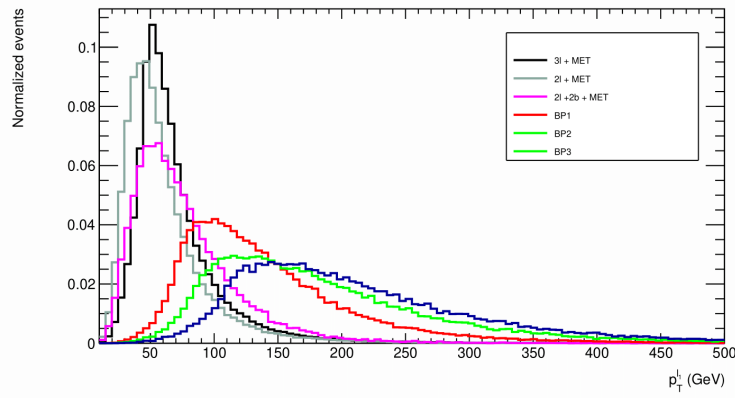
- C_1 : The $l^+l^- + \cancel{E}_T$ and $l^+l^-l^\pm + \cancel{E}_T$ backgrounds feature naturally feature an opposite sign same flavor (OSSF) dilepton peak around $M_Z = 91.2$ GeV owing to the involvement of at least one on-shell Z . This is not the case with $l^+l^-b\bar{b} + \cancel{E}_T$ since the leptons in this case originate from two different W^\pm thereby leading to the more diffused invariant mass spectrum for dileptons as can be seen in Fig. 7. On the other hand, the signal BPs exhibit distinct $\mu\mu$ dilepton peaks around the corresponding M_A values. Given these peaks share little overlap with the Z -peaks in case of the backgrounds, a judicious cut on $M_{\text{inv}}^{\mu\mu}$ can suppress the backgrounds to a great extent. The C_1 cut is therefore applied by demanding $|M_{\text{inv}}^{\mu\mu} - M_A| \leq \Delta M_{\text{inv}}^{\mu\mu}$. We impose $\Delta M_{\text{inv}}^{\mu\mu} = 20$ GeV, 25 GeV and 30 GeV for BP1, BP2 and BP3 respectively upon inspecting the distributions closely.
- C_2 : The heavier the decaying A is, the higher are the p_{Ts} of its daughter $\mu^+\mu^-$. This is clearly reflected in Fig.7 where the $p_T^{\mu_1}$ distribution gets 'harder' upon an increasing M_A . For instance, while the $p_T^{\mu_1}$ spectrum peaks at $\simeq 100$ GeV in case of BP1, the peak shifts to $\simeq 150$ GeV for BP3. Since the background processes have softer $p_T^{\mu_1}$ distributions, an appropriate p_T cut is warranted for each BP for better discernment of the signal. We impose $p_T^{\mu_1} > 60$ GeV, 80 GeV and 100 GeV for BP1-3 respectively.
- C_3 : The presence of the inert particle η_R in the signal final state implies a modified \cancel{E}_T distribution *w.r.t.* the background. We adjust the \cancel{E}_T cut as $\cancel{E}_T > 50$ GeV, 70 GeV and 80 GeV for BP1-3 respectively.

Tables IV-VI elaborate the impact of each cut on the signal and background samples. We refer to the demand of a $\mu^+\mu^-$ pair + b -veto combined with the trigger cuts as the *basic cut*. It is important to point out that the basic cut itself suppresses $\gtrsim 97\%$ of the $t\bar{t}$ leptonic background. Whereas, the same lets $\simeq 62\%$, 64% , 66% of the signal samples corresponding to BP1, BP2 and BP3 respectively to pass through. Further, the di-muon invariant mass cut is also shown to hugely effective in this regard. In fact, its efficacy progressively increases from in going from BP1 to BP3. And this can be traced back to sparsely populated $M_{\text{inv}}^{\mu\mu}$ bins in case of the backgrounds. We add here that in case of all the signal BPs, the invariant mass cut retains $\simeq 90\%$ of the events that pass the basic cut.

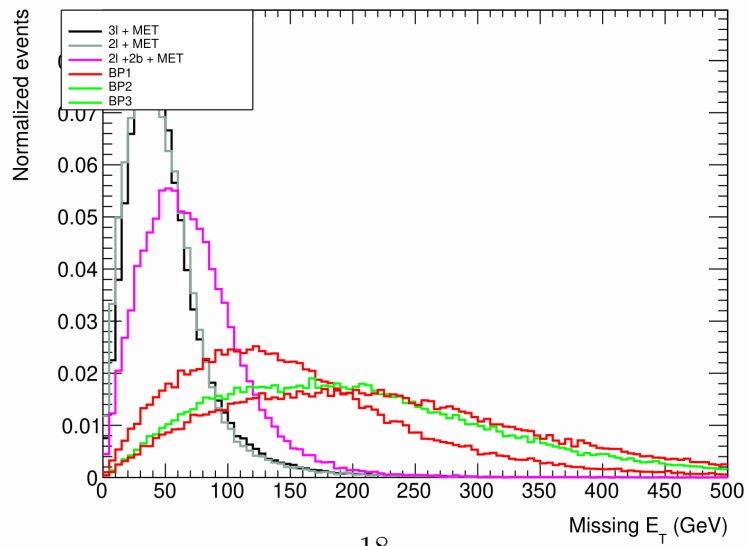
With the completion of the cut-based analysis, we turn to the multivariate analysis (MVA) using Decorrelated Boosted Decision Tree (BDTD) algorithm as implemented within the Toolkit for Multivariate Data Analysis (TMVA) [52] framework. A brief overview of the method is in order. To classify an events as signal-like or background-like, decision trees



(a)



(b)



(c)

BP1	Yield at 300 fb ⁻¹			
	Basic cut	C_1	C_2	C_3
Signal	2450	2192	2129	1949
$2l + \cancel{E}_T$	116020	11590	7985	3080
$2l + 2b + \cancel{E}_T$	247319	34258	29207	18772
$3l + \cancel{E}_T$	13029	374	262	106
$N_S^{\text{CB}} = 1949$		$N_B^{\text{CB}} = 21958$		

TABLE IV: Signal and background yields corresponding to BP1 surviving the trigger and selection cuts for $L = 300 \text{ fb}^{-1}$.

BP2	Yield at 300 fb ⁻¹			
	Basic cut	C_1	C_2	C_3
Signal	666	591	565	522
$2l + \cancel{E}_T$	116020	9943	4495	1056
$2l + 2b + \cancel{E}_T$	247319	31327	21519	9212
$3l + \cancel{E}_T$	13029	330	155	46
$N_S^{\text{CB}} = 522$		$N_B^{\text{CB}} = 10314$		

TABLE V: Signal and background yields corresponding to BP2 surviving the trigger and selection cuts for $L = 300 \text{ fb}^{-1}$.

are used as classifiers. One discriminating kinematic variable with an optimised cut value applied on it is associated with each node of the decision tree, to make the best possible distinction between the signal-like and background-like events. The handle to do this within TMVA is to tune the BDTD variable `NCuts`. The training of the decision trees starts from a zeroth node and continues till a particular depth specified by the user is reached. This particular depth is termed as `MaxDepth`. Finally from the final nodes or the leaf nodes, an event can be specified as signal or background according to their purity. An event can be tagged as signal (background) when $p > 0.5$ ($p < 0.5$).

Now the decision trees are considered weak classifiers as they are prone to statistical fluctuations of the training sample. To circumvent this problem, one can combine a set of weak classifiers into a stronger one and create new decision trees by modifying the weight of the events. This procedure is referred to as Boosting. In this analysis, we choose Adaptive boost with the input variables transforming in a decorrelated manner, since this is very useful for weak classifiers. It is implemented as Decorrelated AdaBoost in TMVA. To avoid over training of the signal and background samples, the result of the Kolmogorov-Smirnov test, i.e. Kolmogorov-Smirnov score (KS-score) is demanded to be always > 0.01 and stable.

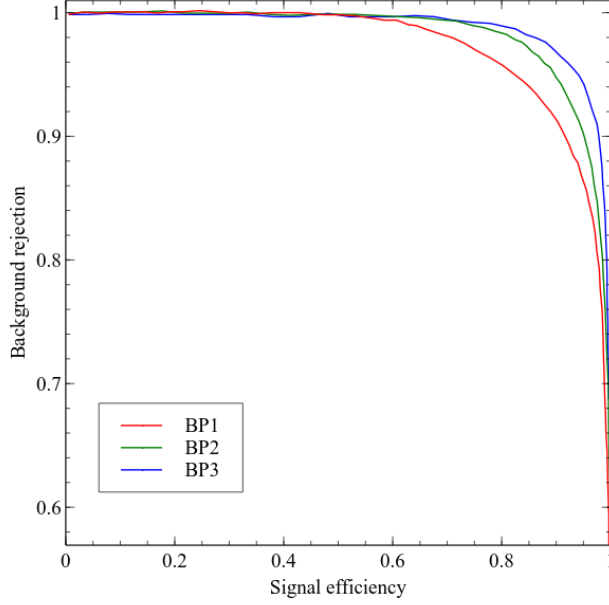


FIG. 8: The ROC curves for the chosen benchmarks. The color coding is given in the legends.

Now the BDTD algorithm orders the kinematic variables that are fed into the algorithm by their importance in discriminating the signal from the background. The following kinematic variables are proposed in this analysis:

$$p_T^{\mu_1}, p_T^{\mu_2}, \eta_{\mu_1}, \eta_{\mu_2}, p_T^{\mu_1\mu_2}, \Delta R_{\mu_1\mu_2}, M_{\text{inv}}^{\mu\mu}, \cancel{E}_T.$$

In the above, $p_T^{\mu_1\mu_2}$ straightforwardly refers to the *vector* transverse momentum of the di-muon system, i.e., $p_T^{\mu_1\mu_2} \equiv \sqrt{(p_x^{\mu_1} + p_x^{\mu_2})^2 + (p_y^{\mu_1} + p_y^{\mu_2})^2} = p_T^A$. The variables that turn out to be the most important in BDT ranking are $p_T^{\mu_1}, p_T^{\mu_2}, \eta_{\mu_1}, \eta_{\mu_2}, p_T^{\mu_1\mu_2}, \Delta R_{\mu_1\mu_2}, M_{\text{inv}}^{\mu\mu}, \cancel{E}_T$. The relevant BDT parameters are tabulated in Table VII. The signal and background distributions along with their KS-scores are depicted in Fig.10 in the Appendix. The degree of background rejection for each BP can be gauged from the Receiver's Operative Characteristic (ROC) curves as shown in Fig.8. The efficiency of background rejection is seen to improve sequentially from BP1 to BP3. And this trend is only expected on account of the progressively smaller overlap recorded between the signal BPs and the background upon increasing M_A . The yields for signal benchmarks and corresponding backgrounds after optimisation through BDTD-analysis are given in Table VIII.

A comparison between the numbers in Tables IV-VI and Table VIII reveals that background rejection following the BDT analysis is manyfold better than what is obtained from the cut-based analysis. And this is seen to be consistently true for all the signal BPs. The

BP3	Yield at 300 fb ⁻¹			
	Basic cut	C_1	C_2	C_3
Signal	454	414	393	360
$2l + \cancel{E}_T$	116020	5436	2319	447
$2l + 2b + \cancel{E}_T$	247319	17798	11247	4130
$3l + \cancel{E}_T$	13030	183	70	18
$N_S^{\text{CB}} = 360$		$N_B^{\text{CB}} = 4595$		

TABLE VI: Signal and background yields corresponding to BP1 surviving the trigger and selection cuts for $L = 300 \text{ fb}^{-1}$.

BP	Ntrees	MinNodeSize	MaxDepth	NCuts	KS-score for signal (background)	BDT Score
BP1	140	3	3	37	0.233 (0.239)	0.3135
BP2	140	3	4	20	0.461 (0.046)	0.4459
BP3	150	3	3	25	0.743 (0.44)	0.3646

TABLE VII: Tuned BDT parameters for BP1, BP2, BP3

BP1			BP2		
	Process	Yield at 300 fb ⁻¹		Process	Yield at 300 fb ⁻¹
Background	$2l + \cancel{E}_T$	253	Background	$2l + \cancel{E}_T$	35
	$2l + 2b + \cancel{E}_T$	503		$2l + 2b + \cancel{E}_T$	39
	$3l + \cancel{E}_T$	29		$3l + \cancel{E}_T$	~ 2
	N_B^{BDT}	785		N_B^{BDT}	76
N_S^{BDT}		1131	N_S^{BDT}		275

BP3		
	Process	Yield at 300 fb ⁻¹
Background	$2l + \cancel{E}_T$	50
	$2l + 2b + \cancel{E}_T$	47
	$3l + \cancel{E}_T$	~ 3
	N_B^{BDT}	100
N_S^{BDT}		236

TABLE VIII: The signal and background yields at 300 fb⁻¹ for BP1, BP2 and BP3 for the $\mu^+\mu^- + \cancel{E}_T$ channel as obtained from the BDTD analysis.

BDT then accordingly outperforms cut-based in case of the signal observability. We show the variation of the signal significance with the integrated luminosity in the two cases in Fig.9. For example, a traditional cut-based approach predicts a 5σ discovery for BP3 with $L \simeq 273 \text{ fb}^{-1}$. On the other hand, the BDT predicts the same statistical significance for

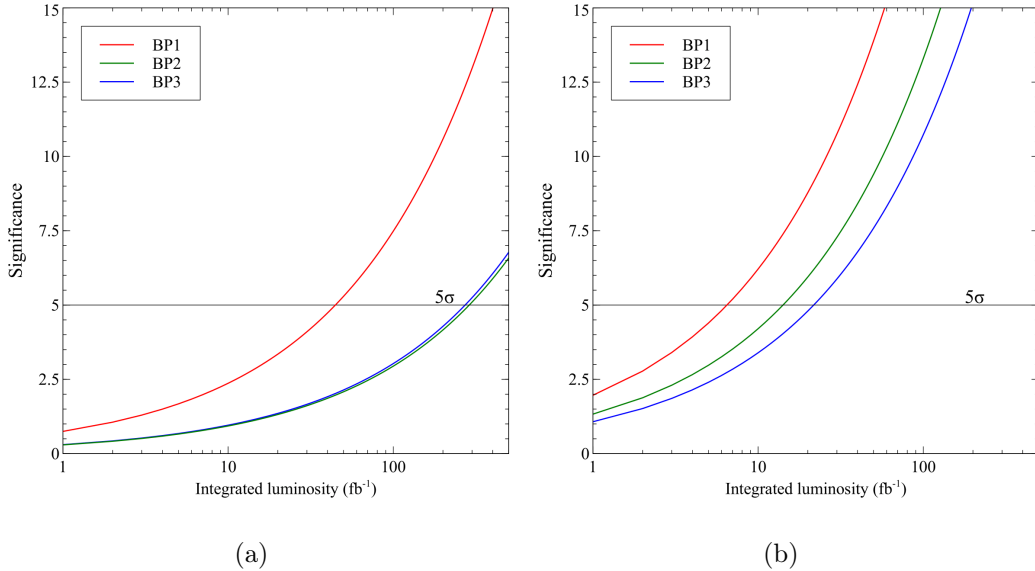


FIG. 9: Variation of the signal significance S versus the integrated luminosity L for the (a) cut-based and (b) multivariate analysis.

$L \simeq 22 \text{ fb}^{-1}$. Such a healthy statistical yield clearly makes the present scenario testable at the early 14 TeV runs of the LHC.

VI. CONCLUSIONS

The Type-X 2HDM is long known to accommodate the observed excess in muon g-2 for high $\tan\beta$ and a light pseudoscalar A . However, non-observation of $h \rightarrow AA$ at the LHC seriously limits the parameter region. We have augmented the Type-X 2HDM by an additional inert doublet in this work that is endowed with an additional \mathbb{Z}_2 symmetry. We take into account all constraints that are mandated by such a construct and thereafter compute the two-loop Barr-Zee contributions from the inert scalars to Δa_μ . With these additional contributions, we demonstrate that a pseudoscalar mass as large as $M_A \sim 300$ GeV becomes compatible with the observed muon g-2 excess for both the lepton-specific and muon-specific cases. The otherwise constrained parameter region in the M_A - $\tan\beta$ plane obtained in case of the standalone 2HDM thus expands to include much higher M_A .

The $A \rightarrow \mu^+\mu^-$ decay allows for a efficient reconstruction of the pseudoscalar mass. We have probed the collider signal $pp \rightarrow \eta_R \eta_A \rightarrow \eta_R \eta_R A \rightarrow \mu^+\mu^- + \cancel{E}_T$ in this work for the muon-specific case where the di-muon decay mode is dominant. The two salient kinematical features of this signal are found to be the di-muon invariant mass peak that no longer must lie within ~ 100 GeV as in case of the standalone Type-X 2HDM, and, a modified \cancel{E}_T spectrum owing to the presence of inert scalars. In fact, the location of the di-muon invariant mass

peak can possibly discern the given scenario from the Type-X 2HDM. We have performed a detailed analysis of the said signal using both cut-based and multivariate analysis. The multivariate analysis outperforms the cut-based and predicts a 5σ discovery for $M_A \simeq 220$ GeV at $L \simeq 22 \text{ fb}^{-1}$ of the 14 TeV LHC.

Acknowledgments

NC acknowledges support from DST, India, under Grant Number IFA19-PH237 (INSPIRE Faculty Award). NC thanks Indrani Chakraborty for fruitful discussions on TMVA.

VII. APPENDIX

A. Trilinear couplings

$$\lambda_{h\eta^+\eta^-} = v (\sigma_1 c_{\alpha+\beta} - \nu_1 s_\alpha c_\beta + \nu_2 c_\alpha s_\beta), \quad (32a)$$

$$\lambda_{H\eta^+\eta^-} = v (\sigma_1 s_{\alpha+\beta} + \nu_1 c_\alpha c_\beta + \nu_2 s_\alpha s_\beta), \quad (32b)$$

$$\lambda_{A\eta_R\eta_I} = 2v (\sigma_3 c_{2\beta} + (-\kappa_1 + \kappa_2) c_\beta s_\beta), \quad (32c)$$

$$\lambda_{H^+\eta^-\eta_R} = v ((\sigma_2 + \sigma_3) c_{2\beta} + (-\kappa_1 + \kappa_2 - \omega_1 + \omega_2) s_\beta c_\beta), \quad (32d)$$

$$\lambda_{H^+\eta^-\eta_I} = v ((\sigma_2 - \sigma_3) c_{2\beta} + (\kappa_1 - \kappa_2 - \omega_1 + \omega_2) s_\beta c_\beta). \quad (32e)$$

B. Two loop functions

$$\mathcal{F}^{(1)}(z) = \frac{z}{2} \int_0^1 dx \frac{2x(1-x) - 1}{z - x(1-x)} \ln \left(\frac{z}{x(1-x)} \right), \quad (33a)$$

$$\tilde{\mathcal{F}}^{(1)}(z) = \frac{z}{2} \int_0^1 dx \frac{1}{z - x(1-x)} \ln \left(\frac{z}{x(1-x)} \right), \quad (33b)$$

$$\mathcal{F}^{(2)}(z) = \frac{1}{2} \int_0^1 dx \frac{x(1-x)}{z - x(1-x)} \ln \left(\frac{z}{x(1-x)} \right), \quad (33c)$$

$$\mathcal{G}(z^a, z^b, x) = \frac{\ln \left(\frac{z^a x + z^b (1-x)}{x(1-x)} \right)}{x(1-x) - z^a x - z^b (1-x)}. \quad (33d)$$

[1] T. Blum, A. Denig, I. Logashenko, E. de Rafael, B. L. Roberts, T. Teubner, and G. Venanzoni, (2013), [arXiv:1311.2198 \[hep-ph\]](#).

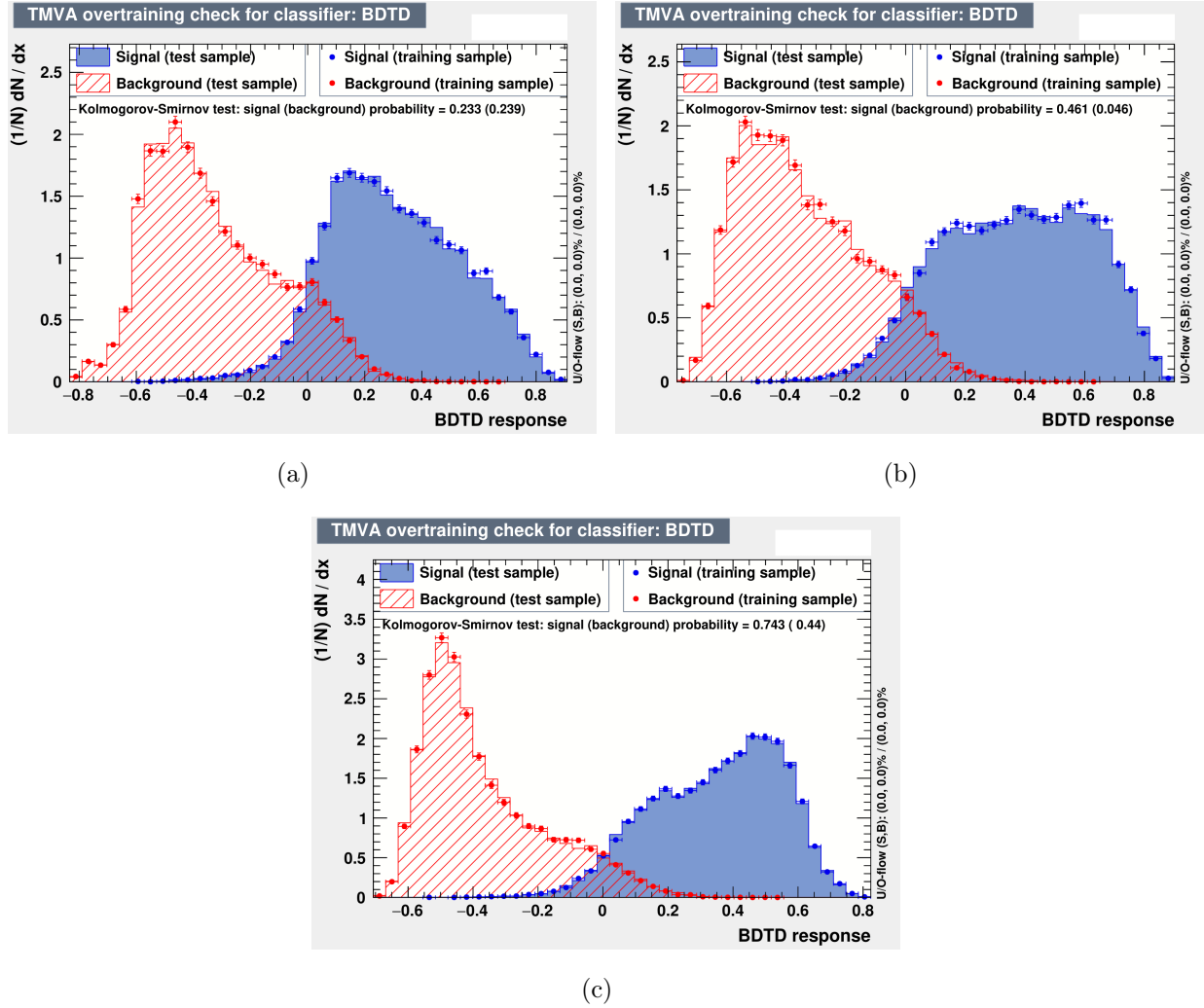


FIG. 10: The KS-scores for the chosen benchmarks

- [2] T. Blum, P. A. Boyle, V. Gülpers, T. Izubuchi, L. Jin, C. Jung, A. Jüttner, C. Lehner, A. Portelli, and J. T. Tsang (RBC, UKQCD), *Phys. Rev. Lett.* **121**, 022003 (2018), [arXiv:1801.07224 \[hep-lat\]](#) .
- [3] A. Keshavarzi, D. Nomura, and T. Teubner, *Phys. Rev. D* **97**, 114025 (2018), [arXiv:1802.02995 \[hep-ph\]](#) .
- [4] M. Davier, A. Hoecker, B. Malaescu, and Z. Zhang, *Eur. Phys. J. C* **80**, 241 (2020), [Erratum: *Eur.Phys.J.C* 80, 410 (2020)], [arXiv:1908.00921 \[hep-ph\]](#) .
- [5] T. Aoyama *et al.*, *Phys. Rept.* **887**, 1 (2020), [arXiv:2006.04822 \[hep-ph\]](#) .
- [6] G. Colangelo, M. Hoferichter, and P. Stoffer, *JHEP* **02**, 006 (2019), [arXiv:1810.00007 \[hep-ph\]](#) .
- [7] M. Hoferichter, B.-L. Hoid, and B. Kubis, *JHEP* **08**, 137 (2019), [arXiv:1907.01556 \[hep-ph\]](#) .
- [8] K. Melnikov and A. Vainshtein, *Phys. Rev. D* **70**, 113006 (2004), [arXiv:hep-ph/0312226](#) .

- [9] M. Hoferichter, B.-L. Hoid, B. Kubis, S. Leupold, and S. P. Schneider, *JHEP* **10**, 141 (2018), [arXiv:1808.04823 \[hep-ph\]](#) .
- [10] T. Blum, N. Christ, M. Hayakawa, T. Izubuchi, L. Jin, C. Jung, and C. Lehner, *Phys. Rev. Lett.* **124**, 132002 (2020), [arXiv:1911.08123 \[hep-lat\]](#) .
- [11] P. A. Zyla *et al.* (Particle Data Group), *PTEP* **2020**, 083C01 (2020).
- [12] G. W. Bennett *et al.* (Muon g-2), *Phys. Rev. D* **73**, 072003 (2006), [arXiv:hep-ex/0602035](#) .
- [13] B. Abi *et al.* (Muon g-2), *Phys. Rev. Lett.* **126**, 141801 (2021), [arXiv:2104.03281 \[hep-ex\]](#) .
- [14] T. Albahri *et al.* (Muon g-2), *Phys. Rev. D* **103**, 072002 (2021), [arXiv:2104.03247 \[hep-ex\]](#) .
- [15] G. C. Branco, P. M. Ferreira, L. Lavoura, M. N. Rebelo, M. Sher, and J. P. Silva, *Phys. Rept.* **516**, 1 (2012), [arXiv:1106.0034 \[hep-ph\]](#) .
- [16] A. Broggio, E. J. Chun, M. Passera, K. M. Patel, and S. K. Vempati, *JHEP* **11**, 058 (2014), [arXiv:1409.3199 \[hep-ph\]](#) .
- [17] J. Cao, P. Wan, L. Wu, and J. M. Yang, *Phys. Rev. D* **80**, 071701 (2009), [arXiv:0909.5148 \[hep-ph\]](#) .
- [18] L. Wang and X.-F. Han, *JHEP* **05**, 039 (2015), [arXiv:1412.4874 \[hep-ph\]](#) .
- [19] V. Ilisie, *JHEP* **04**, 077 (2015), [arXiv:1502.04199 \[hep-ph\]](#) .
- [20] T. Abe, R. Sato, and K. Yagyu, *JHEP* **07**, 064 (2015), [arXiv:1504.07059 \[hep-ph\]](#) .
- [21] E. J. Chun and J. Kim, *JHEP* **07**, 110 (2016), [arXiv:1605.06298 \[hep-ph\]](#) .
- [22] A. Cherchiglia, P. Kneschke, D. Stöckinger, and H. Stöckinger-Kim, *JHEP* **01**, 007 (2017), [Erratum: *JHEP* 10, 242 (2021)], [arXiv:1607.06292 \[hep-ph\]](#) .
- [23] A. Dey, J. Lahiri, and B. Mukhopadhyaya, (2021), [arXiv:2106.01449 \[hep-ph\]](#) .
- [24] D. Chowdhury and O. Eberhardt, *JHEP* **05**, 161 (2018), [arXiv:1711.02095 \[hep-ph\]](#) .
- [25] A. M. Sirunyan *et al.* (CMS), *JHEP* **11**, 018 (2018), [arXiv:1805.04865 \[hep-ex\]](#) .
- [26] E. J. Chun, S. Dwivedi, T. Mondal, and B. Mukhopadhyaya, *Phys. Lett. B* **774**, 20 (2017), [arXiv:1707.07928 \[hep-ph\]](#) .
- [27] E. J. Chun, S. Dwivedi, T. Mondal, B. Mukhopadhyaya, and S. K. Rai, *Phys. Rev. D* **98**, 075008 (2018), [arXiv:1807.05379 \[hep-ph\]](#) .
- [28] S. Iguro, Y. Omura, and M. Takeuchi, *JHEP* **11**, 130 (2019), [arXiv:1907.09845 \[hep-ph\]](#) .
- [29] A. Jueid, J. Kim, S. Lee, and J. Song, *Phys. Rev. D* **104**, 095008 (2021), [arXiv:2104.10175 \[hep-ph\]](#) .
- [30] N. Chen, B. Wang, and C.-Y. Yao, (2021), [arXiv:2102.05619 \[hep-ph\]](#) .
- [31] M. Frank and I. Saha, *Phys. Rev. D* **102**, 115034 (2020), [arXiv:2008.11909 \[hep-ph\]](#) .
- [32] E. J. Chun and T. Mondal, *JHEP* **11**, 077 (2020), [arXiv:2009.08314 \[hep-ph\]](#) .
- [33] S. Moretti and K. Yagyu, *Phys. Rev. D* **91**, 055022 (2015), [arXiv:1501.06544 \[hep-ph\]](#) .
- [34] S. Moretti, D. Rojas, and K. Yagyu, *JHEP* **08**, 116 (2015), [arXiv:1504.06432 \[hep-ph\]](#) .

- [35] M. Merchand and M. Sher, *JHEP* **03**, 108 (2020), [arXiv:1911.06477 \[hep-ph\]](#) .
- [36] Y. Kajiyama, H. Okada, and K. Yagyu, *Nucl. Phys. B* **887**, 358 (2014), [arXiv:1309.6234 \[hep-ph\]](#) .
- [37] T. Abe, R. Sato, and K. Yagyu, *JHEP* **07**, 012 (2017), [arXiv:1705.01469 \[hep-ph\]](#) .
- [38] P. M. Ferreira, B. L. Gonçalves, F. R. Joaquim, and M. Sher, *Phys. Rev. D* **104**, 053008 (2021), [arXiv:2104.03367 \[hep-ph\]](#) .
- [39] A. Djouadi, *Phys. Rept.* **457**, 1 (2008), [arXiv:hep-ph/0503172](#) .
- [40] A. Djouadi, *Phys. Rept.* **459**, 1 (2008), [arXiv:hep-ph/0503173](#) .
- [41] M. Aaboud *et al.* (ATLAS), *Phys. Rev. D* **98**, 052005 (2018), [arXiv:1802.04146 \[hep-ex\]](#) .
- [42] A. M. Sirunyan *et al.* (CMS), *JHEP* **11**, 185 (2018), [arXiv:1804.02716 \[hep-ex\]](#) .
- [43] N. Aghanim *et al.* (Planck), *Astron. Astrophys.* **641**, A6 (2020), [Erratum: *Astron. Astrophys.* 652, C4 (2021)], [arXiv:1807.06209 \[astro-ph.CO\]](#) .
- [44] E. Aprile *et al.* (XENON), *Phys. Rev. Lett.* **119**, 181301 (2017), [arXiv:1705.06655 \[astro-ph.CO\]](#) .
- [45] E. Aprile *et al.* (XENON), *Phys. Rev. Lett.* **121**, 111302 (2018), [arXiv:1805.12562 \[astro-ph.CO\]](#) .
- [46] A. Tan *et al.* (PandaX-II), *Phys. Rev. Lett.* **117**, 121303 (2016), [arXiv:1607.07400 \[hep-ex\]](#) .
- [47] X. Cui *et al.* (PandaX-II), *Phys. Rev. Lett.* **119**, 181302 (2017), [arXiv:1708.06917 \[astro-ph.CO\]](#) .
- [48] J. Alwall, R. Frederix, S. Frixione, V. Hirschi, F. Maltoni, O. Mattelaer, H. S. Shao, T. Stelzer, P. Torrielli, and M. Zaro, *JHEP* **07**, 079 (2014), [arXiv:1405.0301 \[hep-ph\]](#) .
- [49] T. Sjöstrand, S. Ask, J. R. Christiansen, R. Corke, N. Desai, P. Ilten, S. Mrenna, S. Prestel, C. O. Rasmussen, and P. Z. Skands, *Comput. Phys. Commun.* **191**, 159 (2015), [arXiv:1410.3012 \[hep-ph\]](#) .
- [50] J. de Favereau, C. Delaere, P. Demin, A. Giammanco, V. Lemaître, A. Mertens, and M. Selvaggi (DELPHES 3), *JHEP* **02**, 057 (2014), [arXiv:1307.6346 \[hep-ex\]](#) .
- [51] G. Cowan, K. Cranmer, E. Gross, and O. Vitells, *Eur. Phys. J. C* **71**, 1554 (2011), [Erratum: *Eur. Phys. J. C* 73, 2501 (2013)], [arXiv:1007.1727 \[physics.data-an\]](#) .
- [52] A. Hoecker, P. Speckmayer, J. Stelzer, J. Therhaag, E. von Toerne, H. Voss, M. Backes, T. Carli, O. Cohen, A. Christov, D. Dannheim, K. Danielowski, S. Henrot-Versille, M. Jachowski, K. Kraszewski, A. Krasznahorkay, Jr., M. Kruk, Y. Mahalalel, R. Ospanov, X. Prudent, A. Robert, D. Schouten, F. Tegenfeldt, A. Voigt, K. Voss, M. Wolter, and A. Zemla, *ArXiv Physics e-prints* (2007), [physics/0703039](#) .